



PCCP

HCl-H₂O dimer: An accurate full-dimensional potential energy surface and fully coupled quantum calculations of intra- and intermolecular vibrational states and frequency shifts

Journal:	<i>Physical Chemistry Chemical Physics</i>
Manuscript ID	CP-ART-02-2021-000865.R1
Article Type:	Paper
Date Submitted by the Author:	13-Mar-2021
Complete List of Authors:	Liu, Yang; Chongqing University, Li, Jun; Chongqing University, School of Chemistry and Chemical Engineering Felker, Peter; University of California, Los Angeles, Chemistry & Biochemistry Bacic, Zlatko; New York University, Department of Chemistry

SCHOLARONE™
Manuscripts

Cite this: DOI: 10.1039/xxxxxxxxxx

HCl–H₂O dimer: An accurate full-dimensional potential energy surface and fully coupled quantum calculations of intra- and intermolecular vibrational states and frequency shifts[†]

Yang Liu,^a Jun Li,^{*a} Peter M. Felker^{*b} and Zlatko Bačić^{*cd}

Received Date

Accepted Date

DOI: 10.1039/xxxxxxxxxx

www.rsc.org/journalname

The interaction between HCl and H₂O is of considerable theoretical and experimental interest due to its important role in atmospheric chemistry and understanding the onset of the dissociation of HCl in water. In this work, the HCl–H₂O complex is quantitatively characterized in two ways. First, we report a new full-dimensional potential energy surface (PES) for the HCl + H₂O system. The nine-dimensional (9D) PES is based on *circa* 43,000 *ab initio* points calculated at the level of CCSD(T)-F12a/AVTZ with the basis set superposition error correction using the permutation invariant polynomial-neural network method, which can accurately and efficiently reproduce the geometries, energies, frequencies of the complex of HCl with H₂O, as well as the relevant minimum energy path. Next, we present the results of the first fully coupled 9D quantum calculations of the intra- and intermolecular vibrational states of the HCl–H₂O dimer, performed on the new PES. They employ the highly efficient bound-state methodology previously used to compute accurately the rovibrational level structure of the H₂O/D₂O–CO and HDO–CO complexes [P. M. Felker and Z. Bačić, *J. Chem. Phys.*, 2020, **153**, 074107; *J. Phys. Chem. A*, 2021, **125**, 980]. The 9D calculations characterize the vibrationally averaged nonplanar ground-state geometry of the HCl–H₂O complex, the intramolecular vibrational fundamentals of both H₂O and HCl moieties, and their frequency shifts, as well as the low-energy intermolecular vibrational states in each of the intramolecular vibrational manifolds and the effects of the coupling between the two sets of modes. The calculated properties of the HCl–H₂O dimer are in excellent agreement with the available spectroscopic data. The 9D computed dimer binding energy D_0 of 1334.63 cm⁻¹ agrees extremely well with the experimental D_0 equal to 1334 ± 10 cm⁻¹ [B. E. Casterline and A. K. Mollner and L. C. Ch'ng and H. Reisler, *J. Chem. Phys.*, 2010, **114**, 9774]. Moreover, the ground-state expectation value of the out-of-plane bend angle of H₂O, 33.80°, and the computed HCl stretch frequency shift, -157.9 cm⁻¹, both from the 9D calculations, are in very good accord with the corresponding experimental values.

1 Introduction

Mixed (HCl)_{*n*}(H₂O)_{*m*} clusters have attracted a great deal of interest from experimentalists and theorists alike.¹ This attraction stems from the involvement of these complexes in atmospheric chemistry, ozone depletion in particular. Furthermore, small HCl–water clusters provide a microscopic view of the steps that ultimately lead to the fully dissociated HCl in bulk water.^{1,2}

As the smallest of (HCl)_{*n*}(H₂O)_{*m*} clusters, the HCl–H₂O dimer is of considerable significance in its own right. This has made it the subject of numerous high-resolution spectroscopic studies, including microwave spectroscopy,^{3,4} ragout-jet FTIR^{5,6} and infrared (IR) cavity ringdown spectroscopy⁷ in the gas phase, and

^a School of Chemistry and Chemical Engineering, Chongqing University, Chongqing 401331, China; E-mail: jli15@cqu.edu.cn

^b Department of Chemistry and Biochemistry, University of California, Los Angeles, CA 90095-1569, USA; E-mail: felker@chem.ucla.edu

^c Department of Chemistry, New York University, New York, NY, 10003, USA; E-mail: zlatko.bacic@nyu.edu

^d NYU-ECNU Center for Computational Chemistry at NYU Shanghai, 3663 Zhongshan Road North, Shanghai, 200062, China.

[†] Electronic Supplementary Information (ESI) available: [details of any supplementary information available should be included here]. See DOI: 10.1039/b000000x/

IR spectroscopy in liquid helium, as well as nanodroplets.^{8–12} In addition, the vibrational predissociation dynamics of the HCl–H₂O dimer following excitation of the HCl stretch were studied,^{13,14} which led to the first determination of the dimer dissociation energy $D_0 = 1334 \pm 10 \text{ cm}^{-1}$.¹³

Numerous theoretical studies have been performed on the HCl–H₂O dimer.^{15–19} They have established that the equilibrium, minimum-energy structure has a near-linear hydrogen bond where HCl serves as the proton donor to the O atom of water which is the proton acceptor. This global minimum is non-planar, and one of its two symmetrically equivalent pyramidal C_s structures is shown in Figure 1.

An important advance in the theoretical description of the HCl–H₂O dimer was the development of the *ab initio* based nine-dimensional (9D) potential energy surface (PES), of the dimer by Mancini and Bowman,²⁰ constructed by means of a permutationally invariant fit to over 44,000 CCSD(T)-F12b/aug-cc-pVTZ configurations and energies, with the overall root-mean-square error (RMSE) of 24 cm^{-1} . In the following, this PES is referred to as PES-2013. Quantum diffusion Monte Carlo (DMC) calculations performed on this PES²⁰ yielded the dimer's dissociation energy (D_0) value of $1348 \pm 3 \text{ cm}^{-1}$, in good agreement with the experimental result.¹³ The vibrationally averaged ground-state geometry of HCl–H₂O was also characterized.

To date, no rigorous, high-dimensional quantum calculations of excited intra- and intermolecular vibrational states of the HCl–H₂O dimer have been reported. With this in mind, the present article has the following two objectives. The first one is to report a new full-dimensional (9D) PES for this dimer, denoted hereafter as PES-2021. The methodology employed for its construction is similar to that utilized recently to generate the 9D PES for the H₂O–CO interaction.²¹ The HCl–H₂O PES-2021 is based on *circa* 43,000 data points computed at the level of CCSD(T)-F12a/aug-cc-pVTZ with the basis-set-superposition-error (BSSE) correction. The *ab initio* points are fit using the ultraflexible permutation invariant polynomial-neural network (PIP-NN) approach,^{22–24} with the RMSE of only 10.1 cm^{-1} .

The second objective of this paper is to present the results of the first fully coupled 9D quantum calculations of the intra- and intermolecular vibrational states of the HCl–H₂O dimer, utilizing PES-2021. The three intramolecular vibrational fundamentals of the H₂O moiety and the stretch fundamental of the HCl subunit, as well as their frequency shifts from the gas-phase monomer values, are computed, in combination with the low-energy intermolecular vibrational states of the complex within each intramolecular vibrational manifold. The 9D calculations provide a comprehensive and quantitative description of the vibrationally averaged nonplanar ground-state geometry of the dimer, the intra- and intermolecular vibrational levels of the HCl–H₂O complex and the effects of their coupling. The dissociation energy D_0 , the HCl stretch fundamental, and the (vibrationally averaged) out-of-plane bend angle of the H₂O moiety from our 9D quantum calculations on PES-2021 are in excellent agreement with the respective measured values.

What makes these demanding bound-state calculations feasible is the methodology developed in ref. 25, denoted hereafter as I,

which builds on the general approach for high-dimensional, fully coupled computation of intra- and intermolecular (ro)vibrational excitations of noncovalently bound molecular complexes.²⁶ This methodology has two key components. The first one is the surprising insight^{26,27} that for noncovalently bound systems high-energy intramolecular vibrational excitations can be calculated accurately by including in the final basis only a rather small number of low-lying intermolecular eigenstates with energies *far below* those of the intramolecular vibrational states of interest. Of course, this greatly reduces the basis-set size and the computational effort involved.

The second key element is the computational strategy that is particularly well suited to take advantage of the above insight. It involves the partitioning of the full (ro)vibrational Hamiltonian of the dimer,^{25,26} which for HCl–H₂O is 9D, into a (5D) rigid-monomer intermolecular vibrational Hamiltonian, two intramolecular vibrational Hamiltonians – one for the water monomer (3D) and another for the HCl moiety (1D), and a 9D remainder term. Each of the three reduced-dimension Hamiltonians is diagonalized separately and small portions of their low-energy eigenstates are used to build up a compact (9D) product contracted basis covering *all* internal, intra- and intermolecular, degrees of freedom (DOFs). The use of the contracted eigenstate basis for the intermolecular vibrational DOFs is highly advantageous. It makes it straightforward to select just a small number of lowest-energy intermolecular (as well as intramolecular) vibrational eigenstates for inclusion in the compact final 9D product contracted basis,²⁶ in which the full vibrational Hamiltonian of the complex is diagonalized.

This methodology has been already implemented successfully to compute fully coupled intra- and intermolecular (ro)vibrational eigenstates of a number of highly challenging noncovalently bound systems: HF-stretch excited (HF)₂,²⁶ two H₂ molecules in the large clathrate hydrate cage,²⁸ flexible H₂O in C₆₀,²⁹ benzene–H₂O/HDO,³⁰ H₂O/D₂O–CO,²⁵ and HDO–CO.³¹ It is worth noting that H₂O/D₂O–CO²⁵ and HDO–CO³¹, as well as HCl–H₂O in this paper, are the first noncovalently bound molecular complexes with more than four atoms for which all intramolecular vibrational fundamentals, together with low-energy intermolecular vibrational states, have been computed by means of rigorous full-dimensional quantum calculations.

The paper is organized as follows. Section 2 introduces the main components of the development of the full-dimensional PES - *ab initio* methodology and PIP-NN fitting, and describes the key features of the newly developed PES-2021. Section 3 outlines the methodology for full-dimensional and fully coupled quantum calculations of intra- and intermolecular vibrational states of the dimer. The results of these calculations are also presented and discussed in this section. Conclusions are given in Section 4.

2 HCl–H₂O potential energy surface

2.1 *Ab initio* calculations - methodology

All *ab initio* calculations were performed with the 2015.1 version of MOLPRO quantum chemistry program in the current work.³² The explicitly correlated coupled cluster singles, doubles, and per-

turbative triples level^{33,34} associated with the augmented correlation corrected valence double or triple-zeta basis set³⁵ [CCSD(T)-F12a/AVXZ, X= D, T, Q] were employed to determine the geometries, energies and harmonic frequencies of the two stationary points, the non-planar complex well (pyramidal C_s) and the planar C_{2v} , which is a transition state (TS) that connects the two identical complex wells. CCSD(T)-F12a/AVTZ^{33,34} can efficiently provide results close to those computed at the CCSD(T)/AV5Z level^{36,37} and thus has been widely used to develop PESs of many reactive and non-reactive systems.^{20–22,38–44}

In the study of weakly bound complexes, the BSSE often leads to artificial strengthening of interaction well and artificial shortening of intermolecular distance. In this work, the BSSE correction was determined according to the Boys-Bernardi strategy:⁴⁵

$$\Delta E_{\text{BSSE}} = E_{\text{HCl}}^* - E_{\text{HCl}}^\dagger + E_{\text{H}_2\text{O}}^* - E_{\text{H}_2\text{O}}^\dagger, \quad (1)$$

where E^* denotes the energies of HCl or H₂O in the HCl + H₂O basis and E^\dagger refers to energies of HCl or H₂O in their own basis sets. Consequently, the counterpoise (CP) corrected energies were calculated to be

$$E_{\text{CP}} = E_{\text{dimer}} - \Delta E_{\text{BSSE}}. \quad (2)$$

2.2 PIP-NN fitting

The details of constructing the PES of a non-reactive system can be found in our recent work for H₂O and CO.²¹ Firstly, ca. 10 000 points were sampled by varying the distances and orientations between HCl and H₂O to obtain a primitive PES. Specifically, the interaction regions need denser points than the asymptotic region. Therefore, the center-of-mass (COM) distance between HCl and H₂O was varied from 2 to 4 Å with an interval of 0.1 Å and from 4 to 8 Å with an interval of 0.2 Å at different orientations between them. The PES may not provide a reliable description for regions lacking data points, and generally may show some artificial “holes” for these regions. Thus, further data points were added by running quasi-classical trajectory (QCT) calculations on this preliminary PES to explore all relevant dynamic regions. The procedure was repeated to gradually improve the PES until (a) no artificial “hole” was found, and (b) all relevant dynamical results were converged. To eliminate points that are too close to the existing data set, the generalized Euclidean distance between a new point and existing data points were measured. Only those points that are sufficiently far away from each other were added to the existing data set. All permutationally equivalent points (3! = 6) were included in such screenings. Further, the regions near the stationary points and the minimum energy path (MEP) were further sampled to improve the performance of the PES for these regions.

The following NN function form^{22–24} with two hidden layers is used to fit the selected *ab initio* points:

$$V = b_1^{(3)} + \sum_{k=1}^K \left(\omega_{1,k}^{(3)} \cdot f_2 \left(b_k^{(2)} + \sum_{j=1}^J \left(\omega_{k,j}^{(2)} \cdot f_1 \left(b_j^{(1)} + \sum_{i=1}^I \omega_{j,i}^{(1)} \cdot G_i \right) \right) \right) \right) \quad (3)$$

where

$$G_i = \hat{S} \prod_{i < j}^N p_{ij}^{l_{ij}}. \quad (4)$$

The permutation invariant polynomials (PIPs) of the Morse-like variables $p_{ij} = \exp(-\lambda r_{ij})$ (λ is set to 1.0 Å⁻¹ in this work) of internuclear distances between atoms i and j ($i, j = 1 - 5$),^{46,47} shown in eqn (4), are used as the input layer of the NN; \hat{S} is the symmetrization operator that permutes the three identical hydrogen atoms. I in eqn (3) denotes the number of the input PIPs. $\omega_{j,i}^{(l)}$ are weights that connect the i th neuron of $(l - 1)$ th layer and the j th neuron of the l th layer. $b_j^{(l)}$ is the bias of the j th neuron of the l th layer. Both ω and b variables are fitting parameters that need to be determined. J and K are the numbers of neurons in the two hidden layers and f_i ($i = 1, 2$), nonlinear transfer functions for the two hidden layers, were taken as the hyperbolic tangent function, $\tanh(x) = (e^{2x} - 1) / (e^{2x} + 1)$. In the present work, to ensure adequate permutation symmetry,²⁴ the maximum order of the input PIPs is 4, yielding 231 PIPs. The nonlinear least squares fitting method was employed to optimize the fitting parameters (ω and b) by minimizing the RMSE,

$$\text{RMSE} = \sqrt{\sum_{i=1}^{N_{\text{data}}} (E_{\text{output}}^i - E_{\text{target}}^i)^2 / N_{\text{data}}}. \quad (5)$$

To avoid the so called “over-fitting” issue, for each NN fitting the data set was randomly divided into three parts: the training (90%), validation (5%), and test (5%) sets. Different numbers of neurons in the two hidden layers were tested. For each NN architecture, 100 NN trainings with different initial fitting parameters and different training, validation, and test sets were carried out. In accordance with the NN ensemble approach,⁴⁸ the final NN potential was chosen as the average of three best fittings to minimize the random error. The false extrapolation could happen due to the edge points randomly selected in the validation/test sets. Consequently, the fit was chosen only if all three sets (training, validation and test) have similar RMSEs to minimize such possible errors. The maximum deviation was also used as a criterion for selecting the final NN potential.

2.3 *Ab initio* calculations - results

The optimized structures of the HCl and H₂O molecules and the two HCl-H₂O complexes having the planar C_{2v} and pyramidal C_s geometries, respectively, are displayed in Figure 1. The planar C_{2v} structure is the saddle point that connects two symmetry-equivalent pyramidal C_s global minima through two bending angles α and β , also defined in Figure 1. In general, the geometrical parameters from CCSD(T)-F12a/AVTZ and CCSD(T)-F12a/AVQZ calculations are very close to each other. For the H₂O and HCl monomers, these two methods yield essentially the same geometric parameters. For the C_{2v} saddle-point and pyramidal C_s geometry, the CCSD(T)-F12a/AVTZ and CCSD(T)-F12a/AVQZ calculated rigid coordinates within the H₂O and HCl moieties are again consistent with each other. For the hydrogen-bond distance between H₂O and HCl, R_{OH} , the differences between CCSD(T)-F12a/AVTZ and CCSD(T)-F12a/AVQZ results are slightly larger,

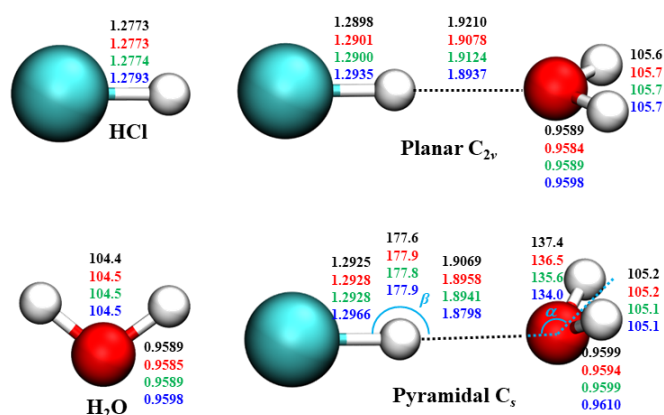


Fig. 1 Comparison of geometries in internal coordinates (distances in Å and angles in deg.) for the stationary points. They correspond to PES-2021, CCSD(T)-F12a/AVQZ, CCSD(T)-F12a/AVTZ, CCSD(T)-F12a/AVDZ, from top to bottom. α presents the angle between H-O (H in HCl) vector and C_2 axis of H₂O. Here and elsewhere, H, Cl, and O atoms are depicted as white, green, and red, respectively.

0.005 and 0.002 Å for the C_{2v} saddle point and pyramidal C_s , respectively. The angle α in the pyramidal C_s shows a deviation of 0.9° between the two methods. The experimentally measured O-Cl distance in the pyramidal C_s is 3.2273 Å,⁴ 0.04 and 0.05 Å longer than the present CCSD(T)-F12a/AVTZ result and the calculation at the CCSD(T)/6-311++G(2d, 2p) level by Alikhani *et al.*¹⁸ The CCSD(T)-F12a/AVTZ-calculated angle α is 135.6°, which is 1.9° larger than that computed at the CCSD(T)/6-311++G(2d, 2p) level,¹⁸ but 9.7° smaller than the measured value.⁴ The reason for this is that the calculated angle corresponds to the equilibrium geometry of the the HCl-H₂O dimer, while the experimental value reflects vibrational averaging over the ground-state wave function. As discussed in Sec. 3.2.1, the present 9D quantum calculations on PES-2021, which incorporate wave function averaging rigorously, yield for this out-of-plane bend angle the value which is in excellent agreement with the experimental result.

Table 1 lists the energies and harmonic frequencies of the stationary points. Notice that all the energies are relative to the isolated monomer (HCl and H₂O) with a center-of-mass (COM) distance of 15 Å. The complete basis set (CBS) calculations were performed by fitting CCSD(T) energy using AVDZ, AVTZ, and AVQZ. As shown in Table 1, the deviations between CCSD(T)-F12a/AVQZ and CCSD(T)-F12a/AVDZ in the energy are 0.47 and 0.52 kcal mol⁻¹, respectively, for the C_{2v} saddle point and the pyramidal C_s . The corresponding deviation in the imaginary harmonic frequency of the C_{2v} saddle point is 0.37 kcal mol⁻¹. The CCSD(T)-F12a/AVTZ computed results are very close to those determined by CCSD(T)-F12a/AVQZ or CCSD(T)/CBS. Therefore, CCSD(T)-F12a/AVTZ is appropriate to develop a global PES for the title system efficiently.

The effect of BSSE is not negligible in this system. At the level of CCSD(T)-F12a/AVTZ, the BSSE contributions for the C_{2v} saddle-point and pyramidal C_s are 0.15 and 0.19 kcal mol⁻¹, respectively. With BSSE corrections, the dissociation energy D_e at the CCSD(T)-F12a/AVTZ level is -5.38 kcal mol⁻¹, close to -5.29

kcal mol⁻¹ determined by CCSD(T)-F12b/AVTZ with BSSE.²⁰ The harmonic zero-point energy (ZPE) of H₂O and HCl calculated by CCSD(T)-F12a/AVTZ is 17.73 kcal mol⁻¹, which is increased to 19.6 kcal mol⁻¹ for the complex well, pyramidal C_s . Using the DMC method, Mancini and Bowman obtained 17.52 and 19.12 kcal⁻¹ for H₂O + HCl and the H₂O-HCl complex well, respectively.²⁰ D_0 based on the harmonic ZPE at CCSD(T)-F12a/AVTZ is 3.50 kcal mol⁻¹, which is 0.37 and 0.35 kcal mol⁻¹ smaller than the experimental measurement by Casterline *et al.*¹³ and the (anharmonic) DMC result by Mancini and Bowman²⁰ using CCSD(T)/CBS/AVXZ (X=D,T,Q,5), respectively. For PES-2021, numerically exact values for D_0 and the ZPE from the fully coupled 9D quantum calculations in this work are reported in Sec. 3.2.1.

2.4 Potential energy surface

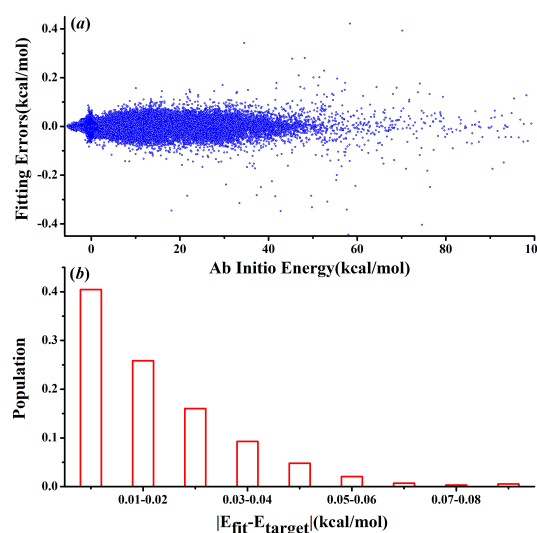


Fig. 2 Upper panel: fitting errors ($E_{\text{fit}} - E_{\text{target}}$, in kcal mol⁻¹) of PES-2021 for the HCl + H₂O system as a function of the ab initio energy (in kcal mol⁻¹). Lower panel: the population of the absolute fitting errors.

Using the strategy mentioned above, approximately 43,000 points were chosen and computed at the level of CCSD(T)-F12a/AVTZ with the BSSE correction. The PIP-NN fitting approach was used to determine the PES. After several tests using different NN architectures with two hidden layers, the final numbers of the neurons in the two hidden layers were chosen to be 20 and 100, respectively, yielding 6821 fitting parameters for each PIP-NN potential. The RMSE of the final PIP-NN PES-2021 is only 0.029 kcal mol⁻¹, based on three best fittings with the RMSEs of 0.034, 0.035, and 0.040 kcal mol⁻¹, respectively. The energies, structures, and harmonic frequencies of the stationary points on the current PES are shown in Figure 1 and Table 1. Good agreement between PES-2021 and CCSD(T)-F12a/AVTZ with BSSE is achieved. Comparing results from PES-2021 and CCSD(T)-F12a/AVTZ with BSSE, the differences for energies and the harmonic frequencies are all within 0.01 kcal mol⁻¹ and 0.04 kcal mol⁻¹, respectively.

The top and bottom panels of Figure 2 present the fitting errors

Table 1 Comparison of the energies E (in kcal mol⁻¹) and harmonic vibrational frequencies (in cm⁻¹) of the stationary points in the HCl + H₂O system.

Species	Note	E		Frequency									
		w/o BSSE	w/BSSE	1	2	3	4	5	6	7	8	9	
HCl+H ₂ O	PES ^a			2990		1646	3830	3939					
	CBS ^b												
	Ab initio ^c	0	0	2988		1647	3834	3944					
	Ab initio ^d			2988		1645	3830	3940					
	Ab initio ^e			2988		1641	3825	3934					
Planar C _{2v}	PES ^a		-5.23	i148	145	149	385	502	1639	2838	3832	3944	
	CBS ^b	-5.41											
	Ab initio ^c	-5.33	-5.28	i149	141	149	388	514	1644	2829	3837	3948	
	Ab initio ^d	-5.39	-5.24	i153	143	150	385	513	1642	2831	3833	3943	
	Ab initio ^e	-5.80	-5.18	i18	153	159	405	542	1636	2813	3827	3937	
Bent C _s	PES ^a		-5.37	143	174	189	440	549	1640	2791	3819	3931	
	CBS ^b	-5.57											
	Ab initio ^c	-5.49	-5.43	146	171	188	455	560	1646	2786	3826	3934	
	Ab initio ^d	-5.57	-5.38	148	175	193	458	562	1644	2787	3821	3929	
	Ab initio ^e	-6.01	-5.34	157	199	208	489	595	1639	2765	3831	3920	

^a This work, PES-2021.

^b This work, CCSD(T)/CBS using energies from AVXZ (X = D, T, Q) based on the CCSD(T)-F12a/AVQZ geometry.

^c This work, CCSD(T)-F12a/AVQZ.

^d This work, CCSD(T)-F12a/AVTZ.

^e This work, CCSD(T)-F12a/AVDZ.

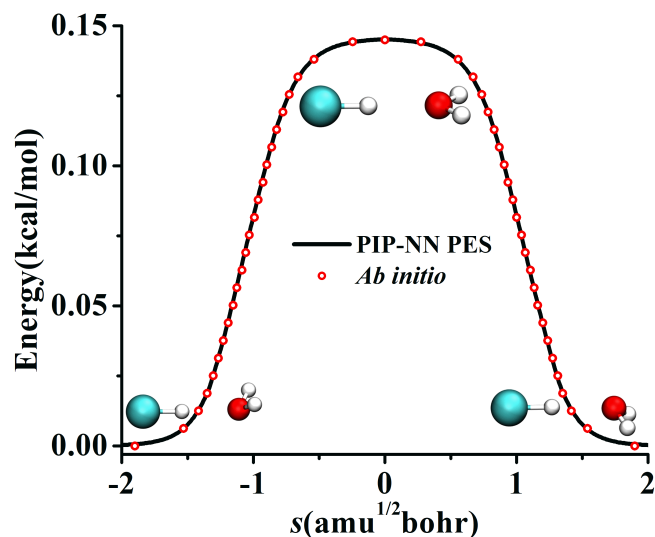


Fig. 3 The potentials of the minimum energy path of the conversion between the planar C_{2v} saddle-point and the pyramidal C_s global minimum on PES-2021 and the corresponding *ab initio* calculation.

as a function of the corresponding CCSD(T)-F12a/AVTZ + BSSE energies and the distributions of the absolute errors, respectively. As can be seen, *circa* 75% data points have fitting errors under 0.02 kcal mol⁻¹. The *ab initio* energies range up to 100 kcal mol⁻¹, which is sufficient for simulations of high-energy or high-temperature dynamics.

Figure 3 shows the potential of the minimum energy path (MEP) along the reaction from the pyramidal C_s to its symmetry-equivalent geometry through the planar C_{2v} saddle-point, which was determined by POLYRATE⁴⁹ program on PES-2021. One can see that PES-2021 reproduces well its corresponding CCSD(T)-F12a/AVTZ calculations with BSSE along the MEP, whose barrier height is extremely low, 0.15 kcal mol⁻¹.

Several one-dimensional (1D) cuts for the interaction energies

between HCl and H₂O with different orientations are displayed in Figure 4. The interaction energies are relative to the asymptote HCl + H₂O. “PIP-NN PES with BSSE” denotes PES-2021 that includes the BSSE correction, “*ab initio* with BSSE” denotes the *ab initio* energies at the level of CCSD(T)-F12a/AVTZ, which contains the BSSE correction, and “*ab initio* without BSSE” denotes the results calculated at CCSD(T)-F12a/AVTZ level that does not include the BSSE correction. One can see that the PES-2021 results are in excellent agreement with the *ab initio* calculations with BSSE correction for all regions, including the repulsive walls, the interaction region, and the asymptotic limit, which indicates the flexibility of the NN fitting approach. Apparently, if the BSSE correction was not included, the interaction well becomes artificially deeper and has a shorter intermolecular distance. The BSSE correction energy ranges up to 0.12 kcal mol⁻¹ in these 1D cuts.

Interaction energies between the H₂O and HCl moieties when they are not at their equilibrium geometries are plotted in Figure 5. Figure 5(a) and Figure 5(b) are for the TS-like configurations, and Figure 5(c) and Figure 5(d) are for the complex well-like configurations. Clearly, with R_{HCl} increased from 1.19 to 1.49 Å, the intermolecular interaction energies become deeper, as shown in Figure 5(a) and Figure 5(c). Figure 5(b) and 5(d) shows the effects of one OH bond length in H₂O on the interaction energies. With the increase of the OH bond length from 0.86 to 1.16 Å, the interaction energies for both configurations are nearly unchanged. Besides, the *ab initio* calculations also agree well with the PES-2021.

Figure 6 presents the polar contour of the interaction energies between HCl and H₂O as functions of R and θ . R denotes the distance between O and H atom of HCl, and θ is the angle between R and the C_{2v} axis of H₂O. Note that HCl and H₂O are kept at their equilibrium geometries and all five atoms are in the same plane. As shown, it is always repulsive when the angle θ is in the range of 90–180°, *i. e.* HCl approaches the H atom of H₂O. It becomes attractive when HCl approaches the O atom of H₂O. The planar

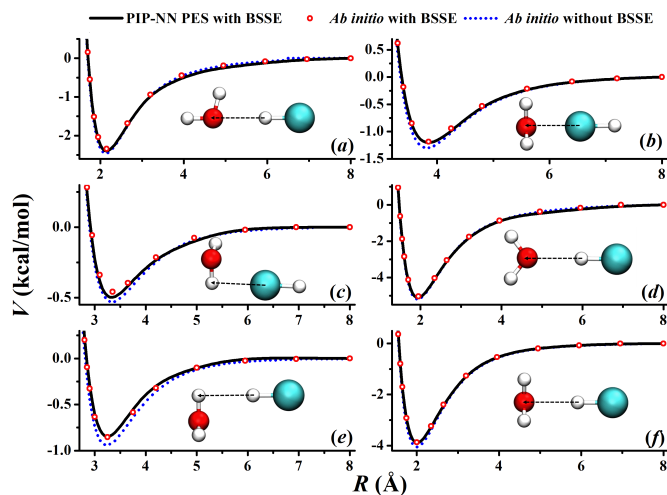


Fig. 4 Comparison of several one-dimensional potential energy cuts as a function of the distance between H₂O and HCl for different collision directions. H₂O and HCl are fixed at their respective equilibrium geometries.

C_{2v} saddle-point is clearly displayed in this figure.

It should be mentioned that the present PES does not specifically describe long-range interactions between the monomers beyond their center-of-mass separation of 8 Å. This would introduce errors in the scattering calculations at low collision energies, which are outside of the scope of the present work. Work is in progress on including a proper description of the long-range interaction in this PES.

The PES generated in this work is available in POTLIB: <http://comp.chem.umn.edu/potlib>.

3 Coupled intra- and intermolecular vibrational states of HCl–H₂O dimer

3.1 Computational methodology

We have reported elsewhere on the 9D calculation of vibrational states in water-diatom complexes in I and in ref. 31. The methodology used in this work is very similar to that of these prior works. As such, we only briefly describe the salient methodological features here and highlight any substantive differences from the preceding studies.

3.1.1 Hamiltonian and coordinates

The H₂O–HCl vibrational ($J = 0$) Hamiltonian that we use is adapted from that derived for a generic molecular dimer by Brocks *et al.*⁵⁰ We write it as

$$\hat{H} = \hat{T}_{inter}(r_0, \omega_A, \omega_B) + \hat{T}^A(\omega_A, \mathbf{q}_A) + \hat{T}^B(\omega_B, r_B) + V(r_0, \omega_A, \omega_B, \mathbf{q}_A, r_B). \quad (6)$$

Here, H₂O is taken as moiety A and HCl as moiety B. The dimer-fixed (DF) frame is defined by assigning the \hat{z}_D axis of the frame to be along the vector \mathbf{r}_0 pointing from the center of mass (c.m.) of A to that of B. The monomer-A-fixed axis frame (MF_A), centered at the c.m. of A, is defined by Radau bisector- z embedding.⁵¹ With the H nuclei of H₂O labeled #1 and #2, the \hat{z}_A axis is taken

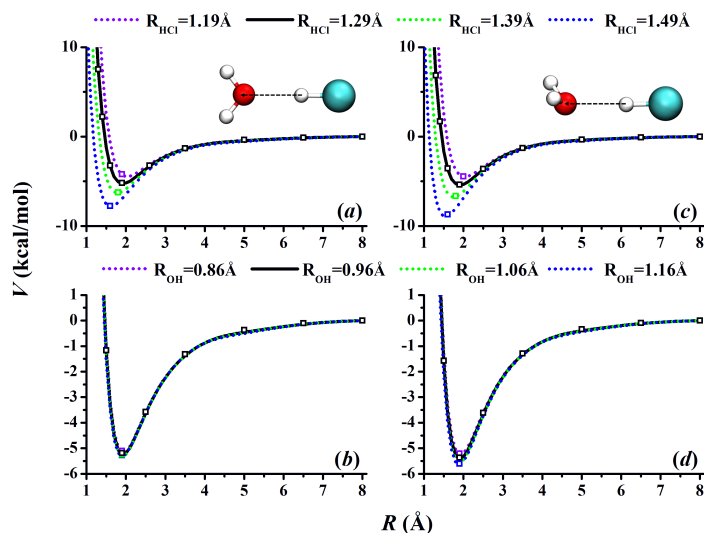


Fig. 5 Potential energy cuts for the planar C_{2v} (in (a) and (b)) and pyramidal C_s (in (c) and (d)) structures along the distance between O and H (in HCl) atoms at different R_{HCl} and R_{OH} (in H₂O) distances. The symbols represent the *ab initio* energies.

to be parallel to the bisector of the Radau vectors \mathbf{R}_1 and \mathbf{R}_2 and pointing toward the O atom. The \hat{y}_A axis is taken to be parallel to $\mathbf{R}_1 \times \mathbf{R}_2$ (i.e., \hat{y}_A is perpendicular to the H₂O plane). And, $\hat{x}_A = \hat{y}_A \times \hat{z}_A$. (Thus, the a , b , and c principal axes of H₂O in its equilibrium geometry correspond to the \hat{x}_A , \hat{z}_A , and \hat{y}_A axes, respectively.) The Euler angles $\omega_A \equiv (\alpha_A, \beta_A, \gamma_A)$ fix the orientation of MF_A with respect to the DF frame. The H₂O vibrational coordinates are the three Radau coordinates R_1 , R_2 , and Θ ,^{52–54} and are collectively denoted \mathbf{q}_A . The MF_B frame, centered at the c.m. of the HCl moiety, is defined by taking \hat{z}_B to be along the vector from the Cl nucleus to the H nucleus. Its orientation is fixed with respect to the DF frame by the two Euler angles $\omega_B \equiv (\alpha_B, \beta_B)$. The HCl vibrational coordinate, corresponding to the distance between the Cl and H nuclei, is labeled as r_B .

The intermolecular kinetic-energy operator, $\hat{T}_{inter}(r_0, \omega_A, \omega_B)$ in eqn 6, is given by

$$\hat{T}_{inter}(\mathbf{Q}) = -\frac{1}{2\mu_0} \frac{\partial^2}{\partial r_0^2} + \hat{J}_A^2 + \hat{J}_B^2 + 2\hat{\mathbf{J}}_A \cdot \hat{\mathbf{J}}_B, \quad (7)$$

where μ_0 is the reduced mass of the dimer, and $\hat{\mathbf{J}}_A$ and $\hat{\mathbf{J}}_B$ are the operators associated with the projections of the rotational angular momenta of monomers A and B, respectively, along the DF axes. $\hat{T}_{inter}(\mathbf{Q})$ is the $J = 0$ version of eqn (2) of I and is adapted from results in ref 50. The monomer-A kinetic-energy operator is the sum of a rotational term $\hat{T}_r^A(\omega_A, \mathbf{q}_A)$, a vibrational term $\hat{T}_v^A(\mathbf{q}_A)$, and a coriolis term $\hat{T}_{cor}^A(\omega_A, \mathbf{q}_A)$. These, adapted from ref. 51, are given, respectively, by eqns (4), (5), and (6) of I. The monomer-B kinetic-energy operator is the sum of a rotational term $\hat{T}_r^B(\omega_B, r_B)$ and a vibrational term $\hat{T}_v^B(r_B)$, which are respectively given by eqns (9) and (10) of I. The 9D PES $V(r_0, \omega_A, \omega_B, \mathbf{q}_A, r_B)$ is the PES-2021 reported in this work. (Note that V is a function of nine coordinates, not ten, since it only depends on the difference between α_A and α_B .)

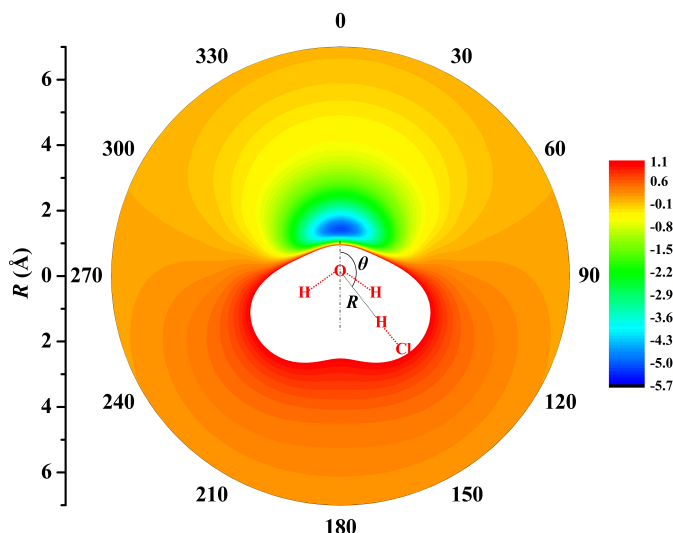


Fig. 6 Polar contour of PES-2021 for HCl + H₂O system as functions of θ and R . The energies are in kcal mol⁻¹ relative to the asymptotic HCl + H₂O with an interval of 0.1 kcal mol⁻¹. The angle OHCl (H in HCl) is kept at 180°.

To solve for the eigenstates of \hat{H} we divide it into four terms, as follows. The 5D (rigid-monomer) intermolecular Hamiltonian, \hat{H}_{inter} , is defined as

$$\hat{H}_{inter}(\mathbf{Q}) \equiv \hat{T}_{inter}(\mathbf{Q}) + \hat{T}_r^A(\omega_A, \mathbf{q}_A^0) + \hat{T}_r^B(\omega_B, r_B^0) + V_{inter}(\mathbf{Q}), \quad (8)$$

where \mathbf{q}_A^0 and r_B^0 are fixed values, close to the equilibrium values, of the pertinent monomer vibrational coordinates, $\mathbf{Q} \equiv (r_0, \omega_A, \omega_B)$ denotes the intermolecular coordinates, and

$$V_{inter}(\mathbf{Q}) \equiv V(\mathbf{Q}, \mathbf{q}_A^0, r_B^0) - V(\mathbf{Q}_\infty, \mathbf{q}_A^0, r_B^0), \quad (9)$$

with \mathbf{Q}_∞ corresponding to a fixed set of intermolecular coordinates with $r_0 = 8.0$ Å, thus representing essentially noninteracting monomers.

The 3D H₂O vibrational Hamiltonian, \hat{H}_v^A is defined as

$$\hat{H}_v^A(\mathbf{q}_A) = \hat{T}_v^A(\mathbf{q}_A) + V^A(\mathbf{q}_A), \quad (10)$$

where

$$V^A(\mathbf{q}_A) \equiv V(\mathbf{Q}_\infty, \mathbf{q}_A, r_B^0), \quad (11)$$

This is the vibrational Hamiltonian of (essentially) isolated H₂O for PES-2021.

The 1D HCl **dimer-adapted** vibrational Hamiltonian is defined as

$$\hat{H}_v^B(r_B) = \hat{T}_v^B(r_B) + V_{DA}^B(r_B). \quad (12)$$

Here,

$$V_{DA}^B(r_B) \equiv V(\mathbf{Q}_0, \mathbf{q}_A^0, r_B). \quad (13)$$

where \mathbf{Q}_0 denotes the values of the intermolecular coordinates associated with the ground state of \hat{H}_{inter} (more on this in Section 3.1.4). Thus, \hat{H}_v^B represents the vibrational Hamiltonian of HCl for the effective 1D potential corresponding to the interaction of flexible HCl with rigid H₂O via a geometry that approximates that of the dimer ground state. This interaction is rather strong,

and therefore the eigenstates of the 1D dimer-adapted Hamiltonian are expected to provide a more compact basis for the HCl stretching coordinate than the vibrational eigenstates of the isolated HCl.

Finally, the fourth term, ΔH , is given by

$$\Delta\hat{H}(\mathbf{Q}, \mathbf{q}_A, r_B) \equiv \hat{H} - \hat{H}_{inter} - \hat{H}_v^A - \hat{H}_v^B. \quad (14)$$

To diagonalize \hat{H} we first compute the low-energy eigenstates of \hat{H}_{inter} , \hat{H}_v^A , and \hat{H}_v^B . We designate these eigenstates as $|\kappa\rangle$, $|\nu_A\rangle$, and $|\nu_B\rangle$, respectively. 9D basis states are then constructed as products of the form

$$|\kappa, \nu_A, \nu_B\rangle \equiv |\kappa\rangle|\nu_A\rangle|\nu_B\rangle, \quad (15)$$

and \hat{H} is diagonalized in this basis. Only the $\Delta\hat{H}$ terms in \hat{H} have off-diagonal matrix elements in this basis. The calculation of these matrix elements is the main challenge in this work.

3.1.2 Calculation of \hat{H}_{inter} eigenstates

We diagonalize \hat{H}_{inter} in a primitive basis composed of states of the form (as adapted from ref. 55):

$$|s, j_A, k_A, m, j_B\rangle \equiv |r_{0,s}\rangle|j_A, k_A, m\rangle|j_B, -m\rangle, \quad (16)$$

where $|r_{0,s}\rangle$, $s = 1, \dots, N_s$ is a potential-optimized discrete-variable representation (PODVR)^{56,57} basis covering the r_0 degree of freedom, the $|j_A, k_A, m\rangle$, $j_A = 0, 1, \dots, j_A^{\max}$, are symmetric-top eigenfunctions dependent on the ω_A , and the $|j_B, -m\rangle$, $j_B^{\max} = 0, 1, \dots, j_B^{\max}$, are spherical harmonics dependent on the ω_B . In this work the basis parameters are as follows: (1) $N_s = 20$ with the $|r_{0,s}\rangle$ DVR points ranging from 2.87 to 5.66 Å, (2) $j_A^{\max} = 10$, and (3) $j_B^{\max} = 18$. The basis includes all of the states with those values of k_A and m that are allowed for each set of j_A and j_B values. This amounts to 527,780 functions.

The $|r_{0,s}\rangle$ PODVR was constructed by first solving the 1D Schrödinger equation

$$-\frac{1}{2\mu_0} \frac{\partial^2 \psi}{\partial r_0^2} + V_{eff}(r_0)\psi = E_0\psi \quad (17)$$

in a sinc-DVR basis consisting of 164 functions centered at quadrature points ranging from 2.43 to 10.53 Å. The $V_{eff}(r_0)$ in eqn (17) is $V_{inter}(\mathbf{Q})$ minimized with respect to all the \mathbf{Q} except r_0 at each one of the r_0 sine-DVR points. The 20 lowest-energy eigenfunctions from eqn (17) were then used to construct the PODVR per refs. 56 and 57.

We diagonalize \hat{H}_{inter} in the eqn-(16) basis by using the Chebyshev version⁵⁸ of filter diagonalization.⁵⁹ The successive operation of \hat{H}_{inter} on a random initial state vector that is required by this algorithm was accomplished as follows. Operation with the kinetic-energy portion of \hat{H}_{inter} was effected by direct matrix-on-vector multiplication, all the relevant matrix elements having been computed prior to such multiplication. For operation with V_{inter} the state vector was transformed to a $(r_0, \cos\beta_A, \gamma_A, \cos\beta_B, (\alpha_A - \alpha_B))$ grid. That representation of the vector was then multiplied by the value of V_{inter} at each grid point. Finally, the result was transformed back to the basis representa-

tion. This procedure is described in detail in I, Section II-3(2). The size of the grid that we employ in this work is 2,323,200 points, which corresponds to 20 r_0 , 12 $\cos\beta_A$, 22 γ_A , 20 $\cos\beta_B$, and 22 ($\alpha_A - \alpha_B$) values, respectively.

H₂O–HCl belongs to the molecular symmetry group $G_4 = [E, (12), E^*, (12)^*]$, where (12) is the water-hydrogen-nucleus interchange operator and E^* is the inversion operator. Thus, the matrix of \hat{H}_{inter} (and \hat{H}) can, in principle, be block-diagonalized into four blocks corresponding to the four irreducible representation (“irreps”) of G_4 . As in I we find it convenient to block diagonalize the matrix into two blocks only, as determined by parity. We accomplish this by projecting out of a random state vector that part which has even or odd parity. We then use that parity-filtered vector as the initial state vector in the filter diagonalization procedure. Hence, the complete diagonalization of \hat{H}_{inter} involves two filter diagonalization runs, one for each parity. While we do not make use of the symmetry of the system with respect to (12) in the diagonalization of \hat{H}_{inter} , we do use it to advantage in the diagonalization of \hat{H} .

The definition of \hat{H}_{inter} (eqn (8)) requires the specification of the \mathbf{q}_A^0 and r_B^0 . For the former we fix the Radau coordinates to $R_1 = R_2 = 0.96753 \text{ \AA}$ and $\cos\Theta = -0.305438605$. (We use the convention of ref. 60 for the definition of the radial Radau coordinates.) These values correspond to a water molecule with OH bond distances of 0.96 \AA and HOH bond angle of 104.52°. For the HCl bond distance, r_B^0 , we use 1.308 \AA . This value is between the expectation values of r_B for the ground- and the first excited-vibrational states of the free HCl monomer. We have determined that this choice produces eigenstates of \hat{H}_{inter} that are close to the intermolecular states associated with the full 9D Hamiltonian \hat{H} . Hence, constructing the 9D basis from the $|\kappa\rangle$ arising from this r_B^0 value leads to desirable convergence properties in the 9D calculations.

3.1.3 Calculation of \hat{H}_v^A eigenstates

The procedure employed here for computing the H₂O vibrational eigenstates (i.e., the diagonalization of \hat{H}_v^A) matches that used to compute the H₂O vibrational eigenstates in I. We use a 3D product DVR basis consisting of two 1D PODVRs^{56,57} covering the R_1 and R_2 Radau coordinates and consisting of eight functions each, and a 1D PODVR covering the $\cos\Theta$ Radau coordinate and consisting of fifteen functions. The matrix of \hat{H}_v^A in this basis was then diagonalized by Chebyshev filter diagonalization.⁵⁸ The 21 lowest-energy eigenstates computed by this procedure were included in the construction of the 9D basis. These include all of the computed H₂O vibrational states less than about 9700 cm^{-1} in energy above the vibrational ground state.

3.1.4 Calculation of \hat{H}_v^B eigenstates

The vibrational eigenstates of H³⁵Cl associated with the dimer-adapted HCl potential – i.e., the eigenstates of \hat{H}_v^B – were computed by direct diagonalization of the matrix of that operator in a PODVR basis consisting of 10 functions. The PODVR was constructed from the eigenstates of \hat{H}_v^B obtained by direct diagonalization of it in a tridiagonal Morse DVR⁵⁶ basis consisting of 25 functions. The Morse potential used to construct the tridiagonal

Morse DVR was taken as

$$V_{\text{Morse}}(r_B) = D \left(1 - \exp^{-\alpha(r_B - r_B^{eq})} \right)^2 \quad (18)$$

where $D = 0.1676914$ hartree, $\alpha = 1.82182 \text{ \AA}^{-1}$, and $r_B^{eq} = 1.275 \text{ \AA}$. The H³⁵Cl reduced mass was taken to be 1784.73 a.u., which corresponds to masses of 1836.153 a.u. and 63727.319 a.u. for the ¹H and ³⁵Cl nuclei, respectively.

To obtain the dimer-adapted HCl potential (i.e., $V_{DA}^B(r_B)$, – see eqn (13)) we used the following values for the components of \mathbf{Q}_0 : $r_0 = 3.273 \text{ \AA}$, $\beta_A = 33.8^\circ$, $\gamma_A = 90^\circ$, $\beta_B = 165.47^\circ$, and $\alpha_A - \alpha_B = 0^\circ$. These correspond closely to the vibrationally averaged geometry of the ground state of \hat{H}_{inter} .

The five lowest-energy eigenstates of \hat{H}_{vib}^B , expressed in terms of the 10-function PODVR basis, were included in the 9D basis. These extend up to about 9900 cm^{-1} above the ground state of \hat{H}_{vib}^B . Notably, the H³⁵Cl fundamental frequency corresponding to the dimer-adapted potential is shifted considerably (about 150 cm^{-1}) to the red of that of free HCl. Quite remarkably, this shift already comes close to matching the redshift from the fully coupled quantum 9D calculations (157.9 cm^{-1} , see Sec. 3.2.2), as well as the experimentally-observed dimer-induced shift of that frequency.^{5,7}

3.1.5 Calculation of the eigenstates of \hat{H}

The matrix of \hat{H} in the 9D basis defined by eqn (15) is block diagonal in the two parity blocks. Given this we constructed two different sets of basis states and performed two different matrix diagonalizations to obtain the 9D eigenstates. Each of these blocks was composed of the same set of H₂O and H³⁵Cl states: the 21 lowest-energy $|\mathbf{v}_A\rangle$ and the five lowest-energy $|\mathbf{v}_B\rangle$. The blocks differ in respect to the 5D \hat{H}_{inter} eigenstates, $|\kappa\rangle$, that were included. For the even-parity basis states we included the 90 lowest-energy $|\kappa\rangle$ with even parity. (These are all the even-parity $|\kappa\rangle$ less than about 870 cm^{-1} above the \hat{H}_{inter} ground state.) For the odd-parity basis states the 90 lowest-energy $|\kappa\rangle$ of odd parity were included. (These are all the odd-parity $|\kappa\rangle$ less than about 930 cm^{-1} above the ground state.) Hence, both of the blocks consist of 9450 states. Such blocks are small enough to allow for direct matrix diagonalization.

The major task in the diagonalization of \hat{H} is the calculation of the matrix elements of the $\Delta\hat{H}$ operator defined in eqn 14. We computed these quantities in the same way as described in Section II E of I. (The method is quite similar to the F matrix approach of Carrington *et al.*^{61,62}). We note that it is at this stage in the overall computational process that we made profitable use of the hydrogen-exchange symmetry of the dimer: That symmetry allows one to reduce the number of $\Delta\hat{H}$ matrix-element calculations by about a factor of two.

3.2 Results and discussion

3.2.1 Vibrationally averaged ground-state geometry and intermolecular vibrational eigenstates

Selected low-energy intermolecular vibrational states of the HCl–H₂O dimer, from the 5D (rigid-monomer) and 9D (full-

Table 2 Low-energy intermolecular states of HCl-H₂O from 5D (rigid-monomer) and 9D calculations (in cm⁻¹). The latter are for HCl and H₂O in their ground intramolecular vibrational states. $\langle r_0 \rangle$ and Δr_0 (in Å) and $\langle \beta_A \rangle$ (in deg) are defined in the text. “Irrep” refers to the irreducible representations of G_4 , for which g/u denote even/odd wavefunction parity and A/B denote symmetric/antisymmetric wavefunction transformation upon water-hydrogen-nuclei exchange. “BSN” means “Basis-state norm” and refers to the 9D results.

N	<i>para</i> $\Delta E : 5D/9D$	<i>ortho</i> $\Delta E : 5D/9D$	$\langle r_0 \rangle$	Δr_0	$\langle \beta_A \rangle$	Irrep	Assignment	BSN
1	0.00 ^a /0.00 ^b		3.273	0.103	33.80	A_g	<i>g.s.</i>	0.993
2		90.71/85.00	3.264	0.103	49.08	B_u	$V_{\text{inversion}}$	0.993
3	131.28/131.94		3.324	0.179	34.11	A_g	V_{stretch}	0.986
4		144.84/146.01	3.269	0.104	37.91	B_g	V_{rock}	0.994
5	221.33/217.29		3.268	0.107	55.46	A_g	$2V_{\text{inversion}}$	0.992
6		221.60/217.00	3.316	0.180	49.38	B_u	$V_{\text{inversion}} + V_{\text{stretch}}$	0.985
7	253.03/249.62		3.261	0.104	51.68	A_u	$V_{\text{inversion}} + V_{\text{rock}}$	0.995
8	255.36/256.73		3.378	0.235	34.61	A_g	$2V_{\text{stretch}}$	0.981
9		273.03/274.85	3.320	0.182	38.27	B_g	$V_{\text{stretch}} + V_{\text{rock}}$	0.990
10	282.88/283.99		3.264	0.107	42.86	A_g	$2V_{\text{rock}}$	0.994
11		338.42/337.22	3.288	0.136	51.39	B_u	?	0.982
12		345.90/343.43	3.359	0.224	49.08	B_u	$V_{\text{inversion}} + 2V_{\text{stretch}}$	0.932
13	349.27/346.60		3.325	0.191	55.18	A_g	$V_{\text{stretch}} + 2V_{\text{inversion}}$	0.984
14	372.60/374.37		3.433	0.280	35.81	A_g	$3V_{\text{stretch}}$	0.978
15	380.69/378.73		3.314	0.187	52.12	A_u	$V_{\text{inversion}} + V_{\text{stretch}} + V_{\text{rock}}$	0.989
16		380.08/379.74	3.275	0.128	53.98	B_g	$V_{\text{rock}} + 2V_{\text{inversion}}$	0.987
17		376.47/382.04	3.287	0.108	47.08	B_u	$3V_{\text{inversion}}$	0.965

^a The ground state of \hat{H}_{inter} is at -1336.66 cm^{-1} relative to the energy of separated rigid monomers evaluated for the q_A^0 and r_B^0 values given in the text.

^b The ground state of \hat{H} is at -1334.63 cm^{-1} relative to the energy of the separated flexible monomers.

dimensional) quantum calculations, for the two monomers in their ground intramolecular vibrational states, are presented in Table 2. Inspection of the results shows that the 9D and 5D intermolecular level energies typically differ by 1-3 cm⁻¹, but for a number of states the energy difference is larger, 4-6 cm⁻¹. This implies that the coupling between the intra- and intermolecular modes of the HCl-H₂O dimer is not negligible, and should be accounted for, even when the monomers are in their ground vibrational states.

From the data reported in Table 2, the binding energy D_0 of the dimer calculated in 9D is 1334.63 cm^{-1} (and 1336.66 cm^{-1} in 5D), which agrees extremely well with the experimental D_0 value of $1334 \pm 10 \text{ cm}^{-1}$.¹³ Thus, for this quantity, PES-2021 yields better agreement with experiment than the PES by Mancini and Bowman,²⁰ for which DMC calculations gave $D_0 = 1348 \pm 3 \text{ cm}^{-1}$. Since the global minimum of PES-2021 is at -1878.2 cm^{-1} , the 9D ZPE of the HCl-H₂O dimer is 543.6 cm^{-1} .

The question of the effective, vibrationally averaged ground-state geometry of the HCl-H₂O complex has received considerable attention.^{3,4,20} As mentioned earlier, the PES of the complex has two symmetrically equivalent global minima corresponding to a nonplanar, pyramidal equilibrium geometry with C_s symmetry, depicted in Figure 1. The minimum-energy path connecting the two C_s minima, shown in Figure 3, exhibits a planar C_{2v} saddle point at the top of the barrier of 49 cm^{-1} separating the minima. Such a low barrier suggests the possibility of the ground-state wave function delocalization over the double-well minimum of the complex, which would result in an effective C_{2v} geometry. Indeed, the DMC calculations on PES-2013 showed the hydrogen atoms of the H₂O moiety as delocalized across the two global minima, resulting in a vibrationally averaged C_{2v} geometry.²⁰

However, the present calculations on PES-2021 arrive at a different conclusion. In our treatment, the deviation of the H₂O

moiety from the planar C_{2v} geometry of the complex is described by β_A , the water polar angle between the C_2 axis of H₂O and the vector \mathbf{r}_0 connecting the c.m. of H₂O to that of HCl. To within a small fraction of a degree, β_A is the complement of the angle θ in Figure 1. Given in Table 2 for each intermolecular state is $\langle \beta_A \rangle$, the expectation value of β_A for that state. It is calculated as $\langle \beta_A \rangle = \cos^{-1} \langle \cos \beta_A \rangle$, where $\langle \cos \beta_A \rangle$ is the expectation value of $\cos \beta_A$ for a given state. In the ground state, $\langle \beta_A \rangle = 33.80^\circ$, which implies that the vibrationally averaged ground-state geometry of the HCl-H₂O dimer is distinctly nonplanar. This $\langle \beta_A \rangle$ is considerably smaller than $\beta_A = 42.8^\circ$ for the equilibrium geometry of the dimer in Figure 1. This means that vibrational averaging plays a significant role in determining the effective geometry of the complex, but the degree of wave function delocalization in the ground state is far from sufficient to yield a planar C_{2v} configuration.

Our calculated $\langle \beta_A \rangle$ of 33.80° agrees remarkably well with the experimentally determined value of 34.7° for this out-of-plane bend angle (denoted ϕ).⁴ Kisiel *et al.* found that statistically much better fits to the experimental rotational constants of the HCl-H₂O dimer could be achieved for this non-planar angle, than by assuming the planar geometry of the complex.⁴ Our result bears out their conclusion.

Also of interest is the hydrogen-bond O-H-Cl angle in the HCl-H₂O dimer. As shown in Fig. 1, its equilibrium value in the pyramidal C_s geometry is 177.6° , very close to the linear arrangement of the three atoms. However, the expectation value of the O-H-Cl angle in the vibrational ground state of the complex is appreciably smaller, 159.2° , with the root-mean-square (rms) amplitude of 10.2° . Thus, the effect of vibrational averaging is significant, as in the case of β_A .

The intermolecular vibrational states in Table 2 are assigned to the fundamentals, first and second overtones, and combinations of three intermolecular modes which are as follows: (1) The in-

version mode, $\nu_{\text{inversion}}$, at 85.00 cm^{-1} (9D), which corresponds to the large-amplitude motion (rotation) of the H_2O moiety about the \hat{x}_A axis (its a principal axis). (2) The intermolecular stretch mode, ν_{stretch} , at 132 cm^{-1} (9D). (3) The water rock mode, ν_{rock} , at 146 cm^{-1} (9D), corresponding to the rotation of the H_2O moiety about the out-of-plane \hat{y}_A axis (its c principal axis).

The assignments of the states in Table 2 in terms of the fundamentals, overtones, and combinations of $\nu_{\text{inversion}}$, ν_{stretch} , and ν_{rock} are made in two ways. One of them is by observing in Table 2 how $\langle\beta_A\rangle$, the expectation value of $r_0 \equiv |\mathbf{r}_0|$, $\langle r_0 \rangle$, and the rms amplitude Δr_0 vary from one state or another. These three quantities are sensitive indicators of the excitation, or lack thereof, of certain intermolecular modes. For example, $\langle\beta_A\rangle$ is equal to 33.8° for the ground state, increasing to 49.08° for the inversion fundamental $\nu_{\text{inversion}}$, and to 55.46° for the inversion overtone $2\nu_{\text{inversion}}$. In contrast, for the stretch and rock fundamentals, ν_{stretch} and ν_{rock} , $\langle\beta_A\rangle$ values are similar to that for the ground state. This makes it straightforward to distinguish states which involve excitation of the inversion mode from those which do not. In the same vein, both $\langle r_0 \rangle$ and Δr_0 increase significantly with the number of quanta in the intermolecular stretch. Their respective values (in Å) are 3.273 and 0.103 for the ground state, 3.324 and 0.179 for ν_{stretch} , 3.378 and 0.235 for $2\nu_{\text{stretch}}$, and 3.433 and 0.280 for $3\nu_{\text{stretch}}$. Excitations of other intermolecular modes cause much smaller changes of $\langle r_0 \rangle$ and Δr_0 .

A complementary way of making the assignments of the computed states is by inspecting contour plots of the reduced probability densities (RPD) associated with the water-c.m.-to-HCl-c.m. vector \mathbf{r}_0 for each in suitably chosen coordinates. Figures 7 and 8 display contour plots of eigenfunction RPDs plotted as a function of the projection of \mathbf{r}_0 along the \hat{x}_A (“x”) and \hat{y}_A (“y”) axes of the water moiety. (The procedure used to generate the RPD contour plots is described in the ESI.†)

Figure 7 shows such plots for the ground state and three members of the inversion-mode progression: $\nu_{\text{inversion}}$, $2\nu_{\text{inversion}}$, and $3\nu_{\text{inversion}}$. Clear nodal patterns make it easy to count the number quanta in the inversion mode, and confirm the assignments made on the basis of changes in $\langle\beta_A\rangle$. The contour plot of the RPD of the ground state, in the top left panel of Figure 7 exhibits two prominent symmetrically placed maxima of the same magnitude, associated with the two equivalent nonplanar vibrationally averaged ground-state geometries of HCl– H_2O having $\langle\beta_A\rangle = 33.80^\circ$.

Figure 8 shows the contour plots of the RPDs of three intermolecular states that involve excitation of the rocking mode of H_2O : ν_{rock} , $2\nu_{\text{rock}}$, and $\nu_{\text{rock}} + 2\nu_{\text{inversion}}$. As shown in Figure 7, the nodal patterns are clear, enabling the assignments of these three states.

In closing this section we consider the progressions of two intermolecular modes. The first one is the inversion mode progression, where the states $\nu_{\text{inversion}}$, $2\nu_{\text{inversion}}$, and $3\nu_{\text{inversion}}$ have energies of 85.0, 217.29, and 382.04 cm^{-1} , respectively. It is easy to see that the energy differences between the neighboring inversion states increase with the increasing number of quanta, which means that the water inversion mode exhibits negative anharmonicity. Next to be considered is the intermolecular stretch progression; the states ν_{stretch} , $2\nu_{\text{stretch}}$, and $3\nu_{\text{stretch}}$ are at 131.94,

256.73, and 374.37 cm^{-1} , respectively. In this case, the energy differences between the successive states decrease slowly with the increasing number of quanta. Thus, the intermolecular stretch shows weak positive anharmonicity, in contrast to the inversion mode with the pronounced negative anharmonicity. For the water rock mode, only two states lie in the energy range covered in Table 2, ν_{rock} at 146.01 cm^{-1} and $2\nu_{\text{rock}}$ at 283.99 cm^{-1} . These two states also show weak positive anharmonicity, like the intermolecular stretch. The large-amplitude water inversion mode stands out for its strong negative anharmonicity.

Experimental data pertaining to the intermolecular vibrational states of the HCl– H_2O complex are not available, precluding for now the comparison with the theoretical results. The latter are therefore predictions which should stimulate further spectroscopic studies of this complex.

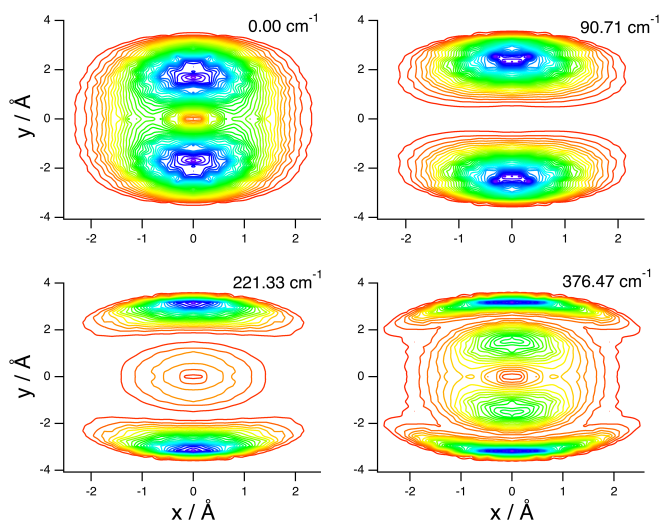


Fig. 7 Contour plots of the reduced probability densities, as a function of the coordinates x and y defined in the text, of the ground state of HCl– H_2O (top left) and the following inversion states in Table 2: (top right) $\nu_{\text{inversion}}$, (bottom left) $2\nu_{\text{inversion}}$, and (bottom right) $3\nu_{\text{inversion}}$.

3.2.2 Intramolecular vibrational eigenstates and frequency shifts

Table 3 displays the results, computational and for the HCl stretch also experimental, pertaining to the intramolecular vibrational excitations of the monomers in the HCl– H_2O dimer and when they are isolated, together with the frequency shifts relative to the isolated monomer values caused by the complexation. The comparison of the second and fifth columns of this table makes it clear that PES-2021 provides a good description of the fundamental excitations of isolated HCl and H_2O , as well as the bend overtone ($2\nu_2$) of H_2O , calculated for the two monomers at a large distance. In the case of the HCl stretch fundamental the agreement between theory and experiment is essentially perfect. For the isolated H_2O , the calculated stretch (ν_1 and ν_3) and bend (ν_2) fundamentals differ from the respective experimental values by no more than 3.5 cm^{-1} ; for the bend overtone ($2\nu_2$) this difference is 4.5 cm^{-1} .

As for the intramolecular vibrational frequency shifts of the

Table 3 Computed (9D calc.) and experimental (Complex expt.) intramolecular vibrational frequencies of HCl-H₂O. The column labeled Monomer calc. gives the intramolecular vibrational excitations of H₂O and HCl calculated on the PES-2021 for a large HCl-H₂O separation. They can be compared to the measured intramolecular vibrational excitations of gas-phase H₂O and HCl (Monomer expt.). Also listed are Δv^{9D} and Δv^{expt} , the calculated (9D) and experimental intramolecular vibrational frequency shifts, respectively. All quantities shown are in cm⁻¹. For additional explanation see the text.

	Monomer calc.	9D calc.	Δv^{9D}	Monomer expt.	Complex expt.	Δv^{expt}
ν_2	1592.35	1595.78	+3.43	1594.75 ^a	–	–
$2\nu_2$	3147.12	3156.70	+9.58	3151.63 ^a	–	–
ν_1	3655.47	3649.97	-5.50	3657.05 ^a	–	–
ν_3	3752.46	3749.85	-2.61	3755.93 ^a	–	–
ν_{HCl}	2885.26	2727.34	-157.92	2885 ^b	2723.1 ^c	-161.9

^a Reference 60.

^b Reference 7.

^c References 5,7.

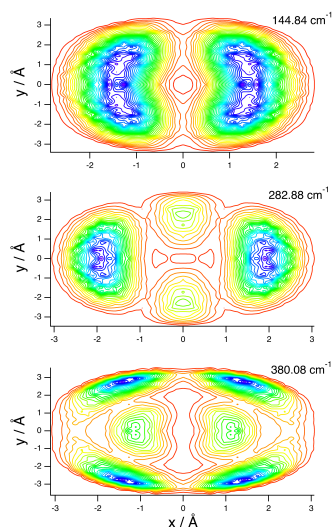


Fig. 8 Contour plots of the reduced probability densities, as a function of the coordinates x and y defined in the text, of the following HCl-H₂O intermolecular states in Table 2: (top) ν_{rock} , (middle) $2\nu_{rock}$, and (bottom) $\nu_{rock} + 2\nu_{inversion}$.

monomers in the HCl-H₂O dimer, the HCl stretch frequency shift (redshift) from the 9D calculations (Δv^{9D}), -157.9 cm⁻¹, is rather large due to hydrogen bonding with H₂O, and agrees very well with the measured HCl stretch redshift in the complex of -161.9 cm⁻¹.^{5,7} In contrast, the 9D frequency shifts (Δv^{9D}) of the H₂O vibrational modes are small. The water stretches ν_1 and ν_3 exhibit redshifts of -5.50 and -2.61 cm⁻¹, respectively. The water bend ν_2 and its overtone $2\nu_2$ are blueshifted by +3.43 and 9.58 cm⁻¹, respectively. The computed frequency shifts are relative to the values calculated for the isolated monomers. The small magnitude of the frequency shifts of the vibrational modes of H₂O is easy to understand. In the dimer, the O atom of H₂O is the proton acceptor, and the two H atoms are free, not involved in the hydrogen bonding with HCl. Consequently, the H₂O vibrations are only weakly perturbed by HCl, resulting in their small frequency shifts.

Unfortunately, no conclusive experimental measurements are available for comparison with the above theoretical results for the H₂O vibrational frequency shifts. The O-H stretching vibrations of HCl-H₂O fall in the highly congested spectral region, where they overlap with the vibrations of pure water clusters.⁶ This makes

reliable assignment of the measured free O-H stretches very difficult, precluding their definitive comparison with theory.

3.2.3 Effects of HCl and H₂O intramolecular excitations on the intermolecular vibrational eigenstates

Tables 4–7 show the energies, computed in 9D, of the fundamentals of the intermolecular modes $\nu_{inversion}$, $\nu_{stretch}$, and ν_{rock} , as well as the overtone $2\nu_{inversion}$, of the HCl-H₂O dimer, in the ν_2 , ν_{HCl} , ν_1 , and ν_3 intramolecular vibrational manifolds, respectively. Comparison of these results with those calculated in 9D for the ground intramolecular vibrational state of the complex in Table 2 reveals how, and to what degree, excitation of different intramolecular modes affects the intermolecular vibrational states of HCl-H₂O.

These effects turn out to be appreciable. The large-amplitude inversion mode $\nu_{inversion}$ is the most sensitive, as the excitation of any of the intramolecular modes changes its energy relative to that in the ground intramolecular vibrational state by 6–16 cm⁻¹. The inversion overtone $2\nu_{inversion}$ exhibits similar sensitivity to intramolecular excitations. It is the excitation of the HCl stretch ν_{HCl} that causes the largest changes in the energies of the intermolecular vibrational modes considered: the $\nu_{inversion}$ energy decreases by 16.3 cm⁻¹, that of $\nu_{stretch}$ increases 5.6 cm⁻¹, and the energy of the ν_{rock} mode increases by 18.5 cm⁻¹. Evidently, the intermolecular vibrational modes of (primarily) the H₂O moiety couple most strongly to the intramolecular ν_{HCl} mode, although their coupling to the intramolecular H₂O vibrations is appreciable as well. Therefore, the coupling between the intra- and intermolecular vibrational modes of the HCl-H₂O dimer has to be taken into account when accurate comparison of theory with experimental data is desired.

Finally, we discuss briefly the last column in Tables 2, 4–7 labeled Basis-state norm (BSN). The entries appearing in this column measure the contribution of the dominant product inter/intra-basis state to the given 9D eigenstate. For the majority of the states shown, the BSN is close to 1, meaning these eigenstates are highly “pure”, i.e., dominated by a single inter/intra-basis state. The exception to this are the states in Table 5, belonging to the ν_{HCl} intramolecular vibrational manifold. For some of them, the BSNs are smaller than 0.9 and even 0.8, indicating appreciable basis-state mixing. This is consistent with the observation above that the ν_{HCl} mode exhibits the strongest coupling to the intermolecular vibrational modes of the H₂O subunit.

Table 4 Low-energy intermolecular states of HCl-H₂O in the ν_2 intramolecular manifold from 9D calculations. ΔE values (in cm⁻¹) are relative to the ν_2 *para* origin at 1595.78 cm⁻¹ above the dimer ground state.

<i>N</i>	<i>para</i> ΔE	<i>ortho</i> ΔE	Irrep	Assignment	Basis-state norm
1	0.000		A_g	origin	0.987
2		93.457	B_u	$\nu_{\text{inversion}}$	0.990
3	131.577		A_g	ν_{stretch}	0.980
4		147.277	B_g	ν_{rock}	0.990
6	232.580		A_g	$2\nu_{\text{inversion}}$	0.987

Table 5 Low-energy intermolecular states of HCl-H₂O in the ν_{HCl} intramolecular manifold from 9D calculations. ΔE values (in cm⁻¹) are relative to the ν_{HCl} *para* origin at 2727.80 cm⁻¹ above the dimer ground state.

<i>N</i>	<i>para</i> ΔE	<i>ortho</i> ΔE	Irrep	Assignment	Basis-state norm
1	0.000		A_g	origin	0.910
2		68.660	B_u	$\nu_{\text{inversion}}$	0.898
3	137.569		A_g	ν_{stretch}	0.777
4		164.509	B_g	ν_{rock}	0.934
6	211.305		A_g	$2\nu_{\text{inversion}}$	0.887

Table 6 Low-energy intermolecular states of HCl-H₂O in the ν_1 intramolecular manifold from 9D calculations. ΔE values (in cm⁻¹) are relative to the ν_1 *para* origin at 3649.97 cm⁻¹ above the dimer ground state.

<i>N</i>	<i>para</i> ΔE	<i>ortho</i> ΔE	Irrep	Assignment	Basis-state norm
1	0.000		A_g	origin	0.984
2		78.724	B_u	$\nu_{\text{inversion}}$	0.981
3	132.158		A_g	ν_{stretch}	0.976
4		144.420	B_g	ν_{rock}	0.989
5	207.616		A_g	$2\nu_{\text{inversion}}$	0.980

Table 7 Low-energy intermolecular states of HCl-H₂O in the ν_3 intramolecular manifold from 9D calculations. ΔE values (in cm⁻¹) are relative to the ν_3 *ortho* origin at 3749.85 cm⁻¹ above the dimer ground state.

<i>N</i>	<i>para</i> ΔE	<i>ortho</i> ΔE	Irrep	Assignment	Basis-state norm
1		0.000	B_g	origin	0.988
2	77.013		A_u	$\nu_{\text{inversion}}$	0.987
3		131.640	B_g	ν_{stretch}	0.979
4	143.655		A_g	ν_{rock}	0.951
5		204.331	B_g	$2\nu_{\text{inversion}}$	0.983

4 Conclusions

In this work we have comprehensively characterized the HCl–H₂O dimer in two ways. First, an accurate full-dimensional (9D) PES for the HCl + H₂O system is developed, based on $\sim 43,000$ *ab initio* points calculated at the level of CCSD(T)-F12a/aug-cc-pVTZ with the BSSE correction. The *ab initio* points are fit using the ultraflexible PIP-NN approach.^{22–24} The resulting 9D PES is designated PES-2021. Two stationary points were determined. One is the global minimum, corresponding to a nonplanar pyramidal geometry and the other one is a planar saddle point that connects two identical global minima. Compared with the *ab initio* calculations, key properties, including geometries, energies, and harmonic frequencies of the stationary points, are well reproduced by PES-2021, thanks to the small root-mean-square error (RMSE) of only 10.1 cm⁻¹. This accurate PES-2021 for the HCl + H₂O system is a reliable platform for future spectroscopic and dynamical simulations.

The newly developed PES-2021 is utilized in this paper for the first fully coupled and full-dimensional quantum bound-state calculations of the intra- and intermolecular vibrational levels of the HCl–H₂O dimer. The calculations rely on the methodology very similar to that employed previously in the quantum 9D calculations of the rovibrational levels of H₂O/D₂O–CO²⁵ and HDO–CO³¹ complexes. It is based on the recently developed general and efficient approach for rigorous computation of the (ro)vibrational bound states of noncovalently bound binary molecular complexes,²⁶ which exploits the insight that their high-energy intra- and low-energy intermolecular vibrational modes are coupled extremely weakly.^{26,27}

Following refs. 25 and 31, the full 9D vibrational Hamiltonian of the HCl–H₂O dimer is partitioned into three reduced-dimension Hamiltonians - the 5D rigid-monomer intermolecular vibrational Hamiltonian and two intramolecular vibrational Hamiltonians, one for the H₂O moiety (3D) and another for the HCl monomer (1D), as well as the 9D remainder term. The three reduced-dimension Hamiltonians are diagonalized separately and small portions of their low-energy eigenstates are used to build up a compact 9D product contracted basis covering all internal, intra- and intermolecular DOFs, in which the matrix of full vibrational Hamiltonian of the complex is diagonalized directly.

The 9D calculations yield the HCl–H₂O dimer binding energy D_0 of 1334.63 cm⁻¹, in excellent agreement with the experimental $D_0 = 1334 \pm 10$ cm⁻¹.¹³ They also result in the nonplanar vibrationally averaged geometry of the dimer, with the computed ground-state expectation value of the out-of-plane bend angle of the H₂O, $\langle \beta_A \rangle$, equal to 33.80°. Again, this theoretical result agrees very well with the spectroscopically determined value of 34.7°.⁴

In the energy range of about 380 cm⁻¹ above the ground state, the excited intermolecular vibrational states are assigned to the fundamentals, first and second overtones, and combinations of three intermolecular modes: the water inversion mode, the intermolecular stretch mode, and the water rock mode. The progressions in the inversion and intermolecular-stretch modes with up to three quanta of excitation exhibit negative and positive anhar-

monicities, respectively.

Pertaining to the intramolecular vibrational excitations of the HCl–H₂O dimer and their frequency shifts relative to the isolated monomer values, the HCl stretch frequency shift (redshift) from the 9D calculations is -157.9 cm⁻¹. It is rather large owing to hydrogen bonding with H₂O (where HCl is the proton donor), and in very good agreement with the measured HCl stretch redshift in the complex of -161.9 cm⁻¹.^{5,7} On the other hand, the H₂O vibrational modes display either small redshifts (the stretches ν_1 and ν_3) or small blueshifts (the bend ν_2 and its overtone $2\nu_2$). This is readily understood from the fact that the two H atoms of water do not participate in the hydrogen bonding with HCl.

The 9D calculations also reveal that the excitation of different intramolecular modes of the HCl–H₂O dimer affects measurably the energies of the intermolecular vibrational states. The intermolecular vibrational modes largely involving the H₂O moiety, the inversion mode in particular, couple most strongly to the intramolecular HCl stretch, not surprising given its direct involvement in hydrogen bonding. This manifests in appreciable changes of the energies of the former upon excitation of the HCl stretch mode.

We hope that the comprehensive theoretical results in this paper will motivate new spectroscopic investigations of the HCl–H₂O dimer, aimed especially at its intermolecular vibrations for which currently there are no experimental results. In the near future, our quantum 9D calculations will be extended to the $J = 1$ rovibrational levels of the HCl–H₂O dimer, as well as those of other isotopologues, e.g., HCl–D₂O⁶ and DCl–D₂O.⁷

Conflicts of Interest

There are no conflicts of interest to declare.

Acknowledgements

Y.L. and J.L. have been financially supported by National Natural Science Foundation of China (Contract Nos. 21973009) and Chongqing Municipal Natural Science Foundation (Grant No. cstc2019jcyj-msxmX0087). Z.B. is grateful to the National Science Foundation for its partial support of this research through the Grant CHE-1566085. P.F. is grateful to Prof. Daniel Neuhauser for support.

References

- 1 A. K. Samanta, Y. Wang, J. S. Mancini, J. M. Bowman and H. Reisler, *Chem. Rev.*, 2016, **116**, 4913.
- 2 R. P. de Tudela and D. Marx, *Phys. Rev. Lett.*, 2017, **119**, 223001.
- 3 A. C. Legon and L. C. Willoughby, *Chem. Phys. Lett.*, 1983, **95**, 449.
- 4 Z. Kisiel, B. A. Pietrewicz, P. W. Fowler, A. C. Legon and E. Steiner, *J. Phys. Chem. A*, 2000, **104**, 6970.
- 5 M. Weimann, M. Farnik and M. A. Suhm, *Phys. Chem. Chem. Phys.*, 2002, **4**, 3933.
- 6 M. Fárník, M. Weimann and M. A. Suhm, *J. Chem. Phys.*, 2003, **118**, 10120.

- 7 A. J. Honeycutt, R. J. Strickland, F. Hellberg and R. J. Saykally, *J. Chem. Phys.*, 2003, **118**, 1221.
- 8 M. Ortlieb, Ö. Birer, M. Letzner, G. D. Schwaab and M. Havenith, *J. Phys. Chem. A*, 2007, **111**, 12192.
- 9 D. Skvortsov, S. J. Lee, M. Y. Choi and A. F. Vilesov, *J. Phys. Chem. A*, 2009, **113**, 7360.
- 10 S. D. Flynn, D. Skvortsov, A. M. Morrison, T. Liang, M. Y. Choi, G. E. Doublerly and A. F. Vilesov, *J. Phys. Chem. Lett.*, 2010, **1**, 2233.
- 11 A. M. Morrison, S. D. Flynn, T. Liang and G. E. Doublerly, *J. Phys. Chem. A*, 2010, **114**, 8090.
- 12 M. Letzner, S. Gruen, D. Habig, K. Hanke, T. Endres, P. Nieto, G. Schwaab, L. Walewski, M. Wollenhaupt, H. Forbert, D. Marx and M. Havenith, *J. Chem. Phys.*, 2013, **139**, 154304.
- 13 B. E. Casterline, A. K. Mollner, L. C. Ch'ng and H. Reisler, *J. Phys. Chem. A*, 2010, **114**, 9774.
- 14 A. K. Samanta, L. C. Ch'ng and H. Reisler, *Chem. Phys. Lett.*, 2013, **575**, 1.
- 15 M. J. Packer and D. C. Clary, *J. Phys. Chem.*, 1995, **99**, 14323.
- 16 S. Re, Y. Osamura, Y. Suzuki and H. F. Schaefer III, *J. Chem. Phys.*, 1998, **109**, 973.
- 17 G. M. Chaban, R. B. Gerber and K. C. Janda, *J. Phys. Chem. A*, 2001, **105**, 8323.
- 18 M. E. Alikhani and B. Silvi, *Phys. Chem. Chem. Phys.*, 2003, **5**, 2494.
- 19 M. Masia, H. Forbert and D. Marx, *J. Phys. Chem. A*, 2007, **111**, 12181.
- 20 J. S. Mancini and J. M. Bowman, *J. Chem. Phys.*, 2013, **138**, 121102.
- 21 Y. Liu and J. Li, *Phys. Chem. Chem. Phys.*, 2019, **21**, 24101.
- 22 B. Jiang, J. Li and H. Guo, *Int. Rev. Phys. Chem.*, 2016, **35**, 479.
- 23 B. Jiang and H. Guo, *J. Chem. Phys.*, 2013, **139**, 054112.
- 24 J. Li, B. Jiang and H. Guo, *J. Chem. Phys.*, 2013, **139**, 204103.
- 25 P. M. Felker and Z. Bačić, *J. Chem. Phys.*, 2020, **153**, 074107.
- 26 P. M. Felker and Z. Bačić, *J. Chem. Phys.*, 2019, **151**, 024305.
- 27 D. Lauvergnat, P. M. Felker, Y. Scribano, D. M. Benoit and Z. Bačić, *J. Chem. Phys.*, 2019, **150**, 154303.
- 28 P. M. Felker, D. Lauvergnat, Y. Scribano, D. M. Benoit and Z. Bačić, *J. Chem. Phys.*, 2019, **151**, 124311.
- 29 P. M. Felker and Z. Bačić, *J. Chem. Phys.*, 2020, **152**, 014108.
- 30 P. M. Felker and Z. Bačić, *J. Chem. Phys.*, 2020, **152**, 124103.
- 31 P. M. Felker and Z. Bačić, *J. Phys. Chem. A*, 2021, **125**, 980.
- 32 H.-J. Werner, P. J. Knowles, G. Knizia, F. R. Manby, M. Schütz *et al.*, *MOLPRO, version 2015.1, a package of ab initio programs*.
- 33 T. B. Adler, G. Knizia and H. J. Werner, *J. Chem. Phys.*, 2007, **127**, 221106.
- 34 G. Knizia, T. B. Adler and H. J. Werner, *J. Chem. Phys.*, 2009, **130**, 054104.
- 35 T. H. Dunning, Jr., *J. Chem. Phys.*, 1989, **90**, 1007.
- 36 L. Kong, F. A. Bischoff and E. F. Valeev, *Chem. Rev.*, 2012, **112**, 75.
- 37 G. Czako, I. Szabo and H. Telekes, *J. Phys. Chem. A*, 2014, **118**, 646.
- 38 J. Li, S. Carter, J. M. Bowman, R. Dawes, D. Xie and H. Guo, *J. Phys. Chem. Lett.*, 2014, **5**, 2364.
- 39 Y. Liu, M. Bai, H. Song, D. Xie and J. Li, *Phys. Chem. Chem. Phys.*, 2019, **21**, 12667.
- 40 B. Jiang, J. Li and H. Guo, *J. Phys. Chem. Lett.*, 2020, **11**, 5120.
- 41 J. Li, B. Zhao, D. Xie and H. Guo, *J. Phys. Chem. Lett.*, 2020, **11**, 8844.
- 42 D. Lu, J. Behler and J. Li, *J. Phys. Chem. A*, 2020, **124**, 5737.
- 43 D. Lu, J. Li and H. Guo, *CCS Chem.*, 2020, **2**, 882.
- 44 J. Qin and J. Li, *Phys. Chem. Chem. Phys.*, 2021, **23**, 487.
- 45 S. F. Boys and F. Bernardi, *Mol. Phys.*, 2002, **100**, 65.
- 46 C. Qu, Q. Yu and J. M. Bowman, *Annu. Rev. Phys. Chem.*, 2018, **69**, 151.
- 47 Z. Xie and J. M. Bowman, *J. Chem. Theory Comput.*, 2010, **6**, 26.
- 48 Z. H. Zhou, J. Wu and W. Tang, *Artif. Intell.*, 2002, **137**, 239.
- 49 J. L. B. J. Zheng, R. Meana-Paneda, S. Zhang, B. J. Lynch, J. C. Corchado, Y. Y. Chuang, P. L. Fast, W. P. Hu, Y. P. Liu, G. C. Lynch, K. A. Nguyen, C. F. Jackels, A. F. Ramos, B. A. Ellingson, V. S. Melissas, J. Villà, I. Rossi, E. L. Coitino, J. Pu, T. V. Albu, A. Ratkiewicz, R. Steckler, B. C. Garrett, A. D. Isaacson and D. G. Truhlar, *POLYRATE 2016-2A: Computer program for the calculation of chemical reaction rates for polyatomics. University of Minnesota, Minneapolis: 2016*.
- 50 G. Brocks, A. van der Avoird, B. T. Sutcliffe and J. Tennyson, *Molec. Phys.*, 1983, **50**, 1025.
- 51 X. G. Wang and T. Carrington, *J. Chem. Phys.*, 2017, **146**, 104105.
- 52 B. R. Johnson and W. P. Reinhardt, *J. Chem. Phys.*, 1986, **85**, 4538.
- 53 Z. Bačić, D. Watt and J. C. Light, *J. Chem. Phys.*, 1988, **89**, 947.
- 54 B. T. Sutcliffe and J. Tennyson, *Int. J. Quantum Chem.*, 1991, **39**, 183.
- 55 X.-G. Wang and J. T. Carrington, *J. Chem. Phys.*, 2011, **134**, 044313.
- 56 H. Wei and T. Carrington, Jr., *J. Chem. Phys.*, 1992, **97**, 3029.
- 57 J. Echave and D. C. Clary, *Chem. Phys. Lett.*, 1992, **190**, 225.
- 58 V. A. Mandelshtam and H. S. Taylor, *J. Chem. Phys.*, 1997, **106**, 5085.
- 59 M. R. Wall and D. Neuhauser, *J. Chem. Phys.*, 1995, **102**, 8011.
- 60 J. Tennyson, N. F. Zubov, R. Williamson, O. L. Polyansky and P. F. Bernath, *J. Phys. Chem. Ref. Data*, 2001, **30**, 044312.
- 61 M. J. Bramley and T. Carrington, Jr., *J. Chem. Phys.*, 1994, **101**, 8494.
- 62 X. G. Wang and T. Carrington, Jr., *J. Chem. Phys.*, 2002, **117**, 6923.